# Prediction of the non-linear aeroelastic behavior of a cantilever flat plate and equivalent 2D model

Gil, A., Tiseira, A., Quintero, P.* and Cremades, A.

*CMT-Motores Térmicos, Universitat Politècnica de València, Camino de Vera s/n, Valencia, 46022, Spain*

ARTICLE INFO

*Keywords*:
Aeroelasticity
Computational Fluid Dynamics
Fluid Structure Interaction
Non-linear aerodynamics
Unsteady Reynolds Averaged Navier Stokes
Structural Dynamics
Stall flutter

Abstract

Reducing structure weigh is one of the main strategies for decreasing environmental and manufacturing costs of engineering solutions. The reduction in material is normally related with a higher impact of aeroelastic solicitations. For some industrial cases it is needed to account for non-linear aerodynamics and, therefore, the whole fully coupled set of equations needs to be simulated in order to predict its behavior. One possible way of reducing the high computational cost associated with this problem is the use of an equivalent 2D model, whose derivation is not straightforward. This article presents a methodology for reducing the order from a complete three dimensional arbitrary beam to its equivalent 2D characteristic section. The behavior of both systems is analyzed and it is shown how, when the methodology is applied, the resulting 2D system is capable to predict similar results with a computational cost which is reduced by orders of magnitude.

## 1. Introduction

Reduction of production costs and environmental impact is one of the hot topics of modern industry [1]. Decreasing structure material is a common practice for achieving this aim at fields as civil [2], aerospace [3] or automotive [4] engineering. However, reduction in weight is usually related with a decrease in the structural stiffness and could lead to an increase in the importance of aeroelastic effects when the system is exposed to wind loads. As a consequence, an important amount of research has been carried out during past years in order to characterize these phenomena.

Traditionally, aerospace engineering has been the field at which more research efforts have been dedicated to the study of aeroelasticity and the instabilities associated with this kind of Fluid Structure Interaction (FSI). For instance, it is possible to find an important amount of literature quantifying the effects of aeroelastic divergence experimentally [5], analytically [6] or numerically [7]. In addition, references about other related Fluid Structure Interaction phenomena such as flutter [8] or buffeting [9], [10] may be found.

One important simplification widely adopted for the analysis of aeroelasticity is the use of an equivalent 2D section. The advantages of this simplification are clear: the computational cost is lower by orders of magnitude than its equivalent 3D case; the reduction on degrees of freedom ease the interpretation of results and it is possible to obtain closed analytic solutions for inviscid flows. Additionally, the low computational cost allows the study of non-linear aerodynamics using affordable resources. In this sense, Sodja et al. [11] performed a wind tunnel characterization of a 2D airfoil, connected to the tunnel by means of a set of longitudinal and torsional springs of known stiffness; Camilo et al. [12] studied the aeroelastic response of a 2D section using Computational Fluid Dynamics (CFD) to account for aerodynamic non-linearities. However, and despite its undeniable capacity for analyzing this kind of flows, the equivalence between the 2D and the 3D structure is not clear in the literature. Although there exist some rules of the thumb, and there are some proposals for the calculation of equivalent stiffness in classic references, as Dowell [13] (in which it is also possible to find a wide number of analytic solutions for the 2D case), they are limited to a very specific set of structural boundary conditions. Therefore, quantitative extrapolation from the two-dimensional data to the actual three-dimensional structure is not straightforward.

Relative to the simulation of the whole 3D plate, many aeroelastic studies have been carried out. For instance, in the work of Peng and Jinglong [14], a fully coupled three dimensional characterization was

pedquiig@mot.upv.es (Q. P.)
ORCID(s):

performed. The authors solved the Euler and deformable body equations in order to obtain the aeroelastic features of a transport wing flying at low angle of attack. Tsushima and Su [15] performed an aeroelastic analysis over a three dimensional wing. The wing was coupled with a 2D unsteady potential aerodynamic model in order to predict the flutter suppression for flexible wings using piezoelectric effects. Finally, Kwon et al. [16] performed an analysis of the flutter including shock interference effects with a modified small disturbance theory (TSD) as aerodynamic model. Due to the high computational cost of three dimensional calculations, most of the studies performed in the literature tend to use a simplified set of fluid flow equations. In consequence, they are normally limited for evaluating low angles of attack, without noticeable detachments over the body.

Most of the operational life of commercial aircraft will be located at conditions of cruise flight, at which linear or almost linear aerodynamic models can be applicable. Nevertheless, under exigent maneuvers, highly non-linear phenomena could arise, leading to the necessity of accounting for effects which could not be covered with the simplifications named during the previous paragraph. These effects are more noticeable, even at normal operating conditions, in problems related with other industries, such as civil engineering. In this sense, a wide amount of research can be found trying to account for aeroelastic non-linear phenomena. For instance, Wu et al. [17] performed a wind tunnel experiment over a complex section which cannot be modeled using simple aerodynamic theory. In other recent study of Wu et al. [18], the non-linear aerodynamics of a 2D flat plate are analyzed in order to use them for predicting its aeroelastic features. Other related studies which would worth to be cited could be Tang et al. [19], Taylor and Browne [20] or Schellenberg et al. [21]. In these studies, it is also possible to observe how the 2D modeling is adequate in order to analyze aeroelastic phenomena under highly complex aerodynamic conditions. Nevertheless, due to the lack of an accurate 2D equivalence model, 3D characterization is the best tool in order to obtain quantitative data about the actual structure.

The current article attempts to overcome some of these limitations. In first place, a methodology for the obtainment of an equivalent 2D model from an arbitrary 3D geometry will be proposed. Additionally, the simplified model will be corrected in order to account for 3D aerodynamic effects. The limitations of the 2D model will be discussed and, lately, 2D and 3D aeroelastic predictions will be carried out, performing an exhaustive comparison between them. In this sense, in order to ease the interpretation of the current article, the workflow followed during this investigation is sketched at Figure 1.

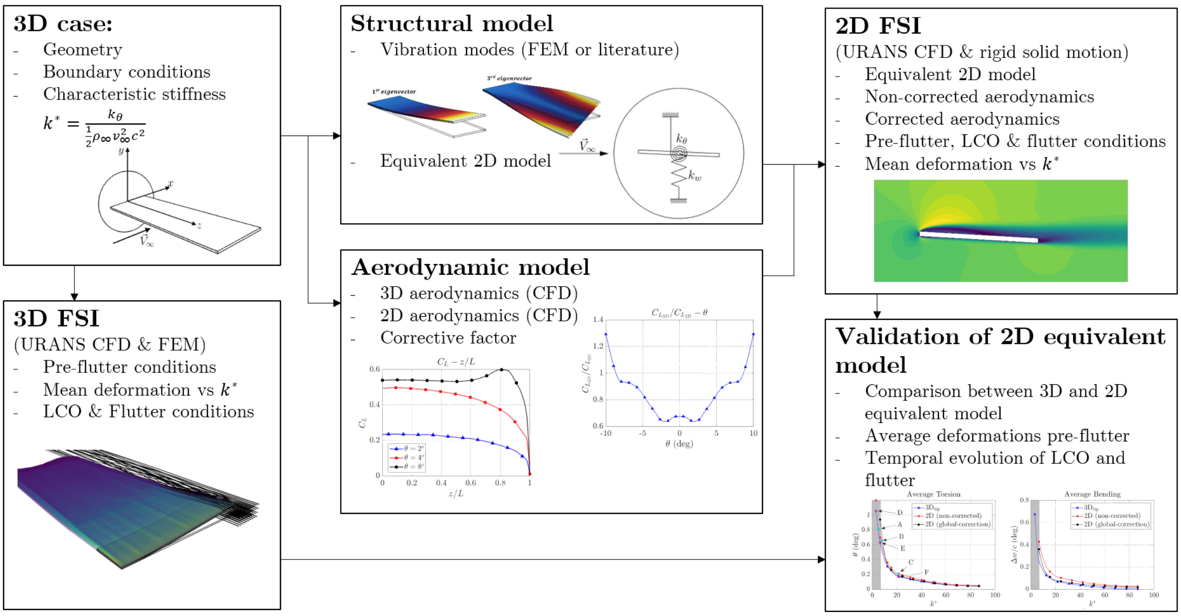


**Figure 1:** Block diagram of the procedure followed during the research

The methodology is applied to a simplified geometry, consisting of a cantilever flat plate immersed in a virtual wind tunnel. The selection of this geometry is due to its main advantages. In first place, the system can be completely defined without many difficulties: (a) its mass and structural features are all well known; (b) the aerodynamic is complex and non-linearities can be identified for very low values of the angle of attack [22]. (c) Despite these complex aerodynamics, the detachment point is always located at the corner of the plate, leading to lift and moment coefficients which are almost independent from the value of the Reynolds number as a first approach [23]. Due to these features, and also to its direct applicability to other problems of the industry, the flat plate has also been studied in similar works by other researchers. It could be worth to reference the works of Gralund et al. [24], Savage and Larose [25] or Attaran et al. [26]. One direct applicability of this geometry can be found to model the structure and aerodynamic of photovoltaic panels and bridges, as it can be observed at the works of Jubayer and Hangan [27], Reina and De Stefano [28] or Larose and Livesey [29].

The paper is structured as follows: Section 2 provides a description of the reference case studied during this work. Section 3 shows the derivation of the equivalent 2D model. This section is illustrated by means of the example of the already mentioned cantilevered plate, although it could be applied to an arbitrary set of boundary conditions and bodies if the derivation conditions are complied with. After that, in Section 4 the methodology for the resolution of the 3D and 2D cases is explained. Then, Section 5 discusses the main results of this study, comparing 3D and 2D, with and without aerodynamic corrections. Finally, Section 6 summarizes the most important results and conclusions.

## 2. Description of the test case

The simulations proposed in this paper are performed on a cantilevered flexible flat plate immersed in a closed channel. The beam is clamped in one of its edges and is let to be free at the other.

The main dimensions of the case of study can be found at Figure 2, which shows a scheme of the problem both in 3D (left) and 2D (right). These are the chord of the plate ($c =$ 100mm), its length ($L = 3.7\ c$) and its thickness ($h = 0.04\ c$), leading to an aspect ratio $AR = 2\ L/c = 7.4$. The channel is conformed by a square section of dimension $H = 4\ c$, with a length of $L_u = 5\ c$ upstream and $L_d = 15\ c$ downstream. Both distances are taken in a manner that the boundary conditions do not significantly affect the computed fluid flow ([30]). Finally, the plate is located at the center of the cross-section of the channel with an incidence of $\theta_0 = 2.5$ deg.

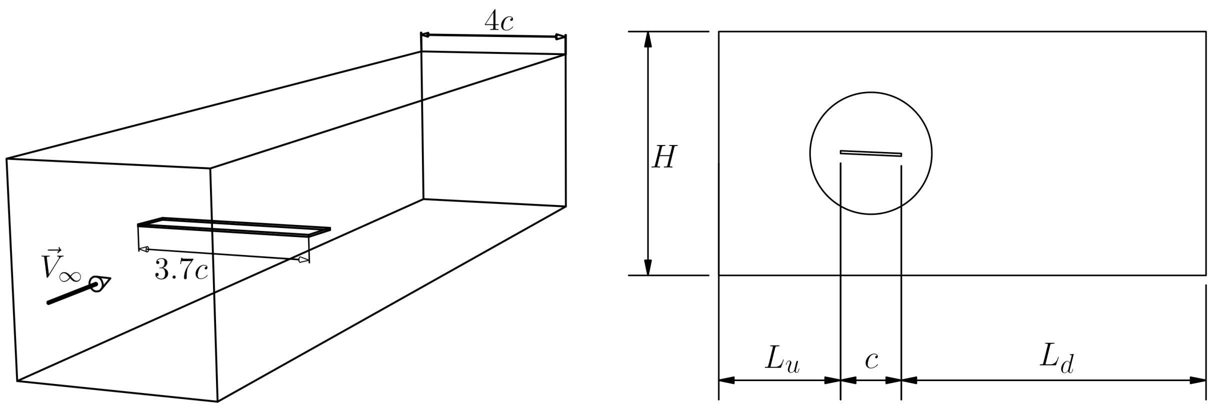


(a) 3D domain (b) 2D domain (not-scale)

**Figure 2:** Domain of the simulation (not scale), 3D plate simulation (left) and 2D simplification of the problem (right)

The walls of the domain are supposed to be placed far enough from the plate in order to assume that the thin boundary layer is not significantly affecting its aerodynamics. The distances have been chosen similar to those studied on the work of Torregrosa et al. [23]. Here, they proposed the use of slip boundary conditions on channel walls in order to decrease the computational cost without jeopardizing the accuracy of the results and, therefore, a similar strategy is followed at the current work. On the other hand, it could be argued that the closeness of the horizontal walls to the plate will make the aerodynamic of the body to be highly influenced by blockage effects. In fact, this is the case. However, as explained during the introduction of the paper, the main aim of this work is to propose a methodology for studying three dimensional geometries (both directly and by means of two dimensional simplifications) using CFD. Therefore, the methodology itself is the main contribution of the article and could also be applied to problems representing a structure lying in a farfield just by increasing these dimensions, although increasing the computational cost of the simulation.

The flow is perpendicular to the inlet section, with a reference constant velocity of $V_\infty = 20\ \mathrm{m\,s^{-1}}$, which is maintained during all the simulations. The fluid is supposed to be air with inlet conditions of density $\rho_\infty = 1.18$ kg m$^{-3}$, viscosity $\mu_\infty = 1.86\cdot10^{-5}$ Pa s and sound speed $a_\infty = 340$ m s$^{-1}$. For the flat plate, the reference material is polymethyl methacrylate, whose mechanical properties are given by its Young Modulus, $E = 3300$ MPa; a Poisson coefficient of $\nu = 0.35$ and a density of $\rho_s = 1180$ kgm$^{-3}$. With these parameters, the flow conditions are given by a Reynolds number of $\mathrm{Re} = \rho_\infty V_\infty c/\mu_\infty \approx 1.5\cdot10^5$ and a Mach number of $\mathrm{Ma} = V_\infty/a_\infty \approx 0.06$. Thus, the flow can be assumed to be incompressible.

It is important to point that the previous values are a reference for the problem. As it will later shown, the stiffness parameter which governs the problem is proportional to $E/(\rho_\infty V_\infty^2)$. Therefore, in order to analyze the influence of this parameter while maintaining the value of Re and Ma, the Young's modulus will be varied during the different simulations.

## 3. Derivation of the 2D equivalent model

In this section, the methodology to reduce a 3D arbitrary beam to an equivalent 2D section is derived. As it is well known, the behavior of the three dimensional system will be governed by the conjunction of the Lagrange equations [31], which can be written as:

$$\frac{d}{dt}\left(\frac{\partial T}{\partial \dot{q}_j}\right) + \frac{\partial U}{\partial q_j} = Q_{q_j} \tag{1}$$

Where $T$ is the kinetic energy of the structure; $q_j$ represents the $j^{th}$ generalized coordinate; $U$ is the potential energy and $Q_{q_j}$ is the generalized force corresponding to the coordinate $q_j$.

As the plate can be structurally modeled as a beam, its displacement could be expressed as a flexural motion, $\Delta w(z,t)$, combined with a torsional displacement, $\Delta\theta(z,t)$. Thus, it would be possible to express each of them as the sum of eigenfunctions, as follows:

$$\Delta\theta(z,t) = \sum_{n=1}^{\infty}\left(\Theta_i(t)\cdot f_i(z)\right) \qquad \Delta w(z,t) = c\cdot\sum_{n=1}^{\infty}\left(W_i(t)\cdot g_i(z)\right) \tag{2}$$

where $f_i(z)$ and $g_i(z)$ are the associated eigenfunctions for torsion and bending, respectively [32] and $\Theta_i(t)$ and $W_i(t)$ are the amplitude associated with each of them. Both functions must comply with the boundary conditions of the structure which, for the case of a clamped-free plate, are $\Delta\theta(0) = \Delta\theta'(0) = 0$; $\Delta w(0) = \Delta w'(0) = 0$ and $\Delta w''(L) = 0$. Figure 3 shows these functions for the flexural and torsional motion for the current set of boundary conditions. The eigenfunctions can be calculated analytically or numerically, as will be explained during the Section 4.

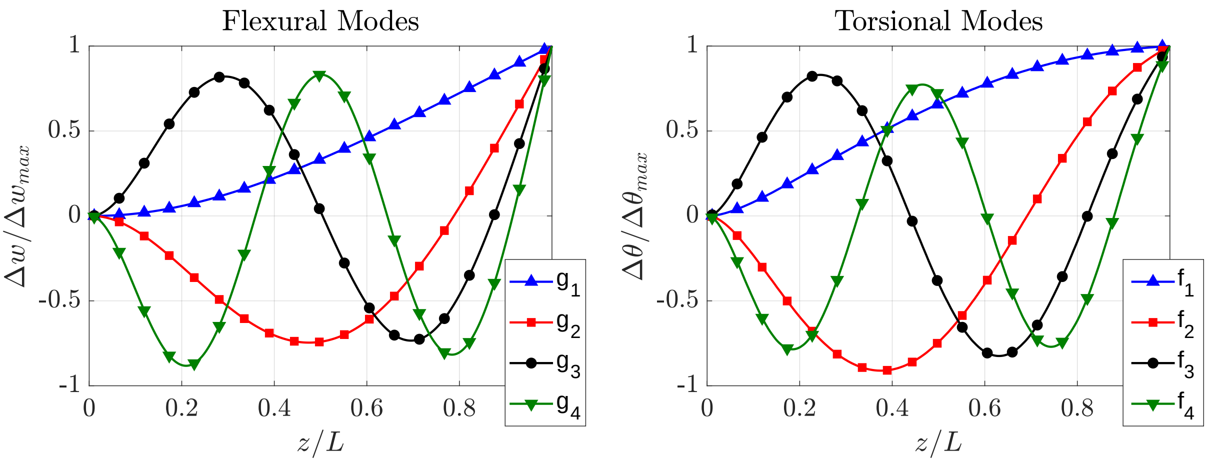


(a) Flexural shape functions (b) Torsional shape functions

**Figure 3:** Normalized deformation modes along the span of the clamped flat plate corresponding to the bending (left) and torsional (right) modes

Once the motion of the plate can be supposed to be a combination of torsional and flexural modes, the vertical displacement and velocity of any point located over the plate ($y_p$) can be, therefore, calculated as equation 3.

$$y_p = -x \sum_{0}^{\infty} \Theta_i(t) \cdot f_i(z) + \sum_{0}^{\infty} W_i(t) \cdot g_i(z) \qquad \dot{y}_p = -x \sum_{0}^{\infty} \dot{\Theta}(t) \cdot f_i(z) + \sum_{0}^{\infty} \dot{W}(t) \cdot g_i(z) \tag{3}$$

where $x$ is the coordinate of the plate in the direction of the chord. $\Theta_i$ and $W_i$ are the torsion and bending coefficients of the series, respectively.

With these assumptions, kinetic, $T$, and potential, $U$, energies of the plate could be expressed following Equation 4:

$$T = \frac{1}{2} \iiint \rho_s \dot{y}_p^2 d\Omega \qquad U = \frac{1}{2} \int GJ \left( \frac{d\, \Delta\theta}{dz} \right)^2 dz + \frac{1}{2} \int EI \left( \frac{d^2\, \Delta w}{dz^2} \right)^2 dz \tag{4}$$

where $G = E/(2 \cdot (1 + \nu))$ is the shear modulus of the material; $J$ is the torsion constant of the section (which, for a rectangular shape with $h/c << 1$ results to be $J = \frac{1}{3}\, c\, h^3$) and $I$ is the second moment of area of the section (which, for a rectangular shape results to be $I = \frac{1}{12}\, c\, h^3$).

Therefore, the left hand term of the Lagrange equations can be written, when a bounded number of $N$ eigenfunctions are considered, and separating the contribution of the flexural and torsional motion, in accordance with Equation 5:

$$\frac{d}{dt}\frac{\partial T}{\partial \dot{\vec{\Theta}}} = \frac{1}{12} \rho_s c^3 h L \mathbf{M}_\theta \ddot{\vec{\Theta}} \qquad \frac{d}{dt}\frac{\partial T}{\partial \dot{\vec{W}}} = \rho_s L c h \mathbf{M}_\mathbf{w} \ddot{\vec{W}} \qquad \frac{\partial U}{\partial \vec{\Theta}} = \frac{GJ}{L} \mathbf{K}_\theta \vec{\Theta} \qquad \frac{\partial U}{\partial \vec{W}} = \frac{EI}{L^3} \mathbf{K}_\mathbf{w} \vec{W} \tag{5}$$

Where $\mathbf{M}_\theta$ and $\mathbf{M}_\mathbf{w}$ are the mass matrices for the torsional and flexural motions, respectively, and $\mathbf{K}_\theta$ and $\mathbf{K}_\mathbf{w}$ are the stiffness matrices for the torsional and flexural motions. Their components can be calculated as stated in Equations 6 and 7. Note that, if eigenfunctions are taken forming an orthogonal base, the terms off of the diagonal will be zero:

$$M_\theta^{ij} = \int_0^1 f_i \left( \frac{z}{L} \right) f_j \left( \frac{z}{L} \right) d \left( \frac{z}{L} \right) \qquad M_w^{ij} = \int_0^1 g_i \left( \frac{z}{L} \right) g_j \left( \frac{z}{L} \right) d \left( \frac{z}{L} \right) \tag{6}$$

$$K_{\theta}^{ij} = \int_{0}^{1} f_i'\left(\frac{z}{L}\right) f_j'\left(\frac{z}{L}\right) d\left(\frac{z}{L}\right) \qquad K_{w}^{ij} = \int_{0}^{1} g_i''\left(\frac{z}{L}\right) g_j''\left(\frac{z}{L}\right) d\left(\frac{z}{L}\right) \tag{7}$$

Finally, it is necessary to obtain the generalized forces. In this sense, the virtual work, $\delta\mathcal{W}$, generated at an arbitrary section will be the combination of the virtual displacement produced by the vertical force (lift) and the virtual torsion produced by the aerodynamic moment. In consequence, Equation 8 can be stated:

$$\frac{d(\delta\mathcal{W})}{dz} = \frac{1}{2}\rho_\infty V_\infty^2 c c_l \cdot \delta w + \frac{1}{2}\rho_\infty V_\infty^2 c^2 c_m \cdot \delta\theta = \frac{1}{2}\rho_\infty V_\infty^2 c c_l \cdot \sum_{1}^{\infty}(\delta W_i g_i) + \frac{1}{2}\rho_\infty V_\infty^2 c^2 c_m \cdot \sum_{1}^{\infty}(\delta\Theta_i f_i) \tag{8}$$

Where $c_l$ and $c_m$ are the aerodynamic coefficients for lift and moment, respectively. Next, in order to obtain an equivalent 2D model by integrating Equation 8, two different assumptions will be made. Namely:

- The aerodynamic coefficients, $c_l$ and $c_m$ are a function only of the local angle of attack and its derivatives of each one of the sections, i.e. the effects of three dimensionality of the aerodynamics can be neglected, as a first approach.
- The aerodynamic force coefficients can be linearized around the rigid angle of attack. The linear term of the serie will be supposed to be constant for the whole span of the plate. This assumption is only valid when the difference between the pitching angle in the tip and the root is low.

With the previous assumptions, the aerodynamic coefficients of equation 8 can be written in a general way, as:

$$c_l = c_l(w_0,\theta_0) + c_{l_\theta}\Delta\theta + \frac{c_{l_w}}{c}\Delta w + \frac{c\cdot c_{l\dot{\theta}}}{V_\infty}\Delta\dot{\theta} + \frac{c_{l\dot{w}}}{V_\infty}\Delta\dot{w} + \sum_{n=2}^{N}\frac{c^n\cdot c_{l\theta^{(n)}}}{V_\infty^n}\Delta\theta^{(n)} + \sum_{n=2}^{N}\frac{c^{n-1}\cdot c_{lw^{(n)}}}{V_\infty^n}\Delta w^{(n)} \tag{9}$$

Being $\Delta\theta^{(n)} = \frac{\partial^n\Delta\theta}{\partial t^n}$ and $\Delta w^{(n)} = \frac{\partial^n\Delta w}{\partial t^n}$. As a consequence, it will be possible to establish the value of the generalized forces as follows:

$$\vec{Q}_{\vec{\Theta}} = \vec{Q}_{\vec{\Theta},0} + \frac{1}{2}\rho_\infty V_\infty^2 c^2 L\mathbf{A}_{\theta,\mathbf{w}}\sum_{0}^{\infty}\frac{c_{m_w^{(n)}}c^{n-1}}{V_\infty^n}\vec{W}^{(n)} + \frac{1}{2}\rho_\infty V_\infty^2 c^2 L\mathbf{A}_{\theta,\theta}\sum_{0}^{\infty}\frac{c_{m_\theta^{(n)}}c^n}{V_\infty^n}\vec{\Theta}^{(n)} \tag{10}$$

$$\vec{Q}_{\vec{W}} = \vec{Q}_{\vec{W},0} + \frac{1}{2}\rho_\infty V_\infty^2 cL\mathbf{A}_{\mathbf{w},\mathbf{w}}\sum_{0}^{\infty}\frac{c_{l_w^{(n)}}c^{n-1}}{V_\infty^n}\vec{W}^{(n)} + \frac{1}{2}\rho_\infty V_\infty^2 cL\mathbf{A}_{\mathbf{w},\theta}\sum_{0}^{\infty}\frac{c_{l_\theta^{(n)}}c^n}{V_\infty^n}\vec{\Theta}^{(n)} \tag{11}$$

where $\mathbf{A}_{\theta,\theta}$, $\mathbf{A}_{\mathbf{w},\theta}$, $\mathbf{A}_{\theta,\mathbf{w}}$ and $\mathbf{A}_{\mathbf{w},\mathbf{w}}$ are the aerodynamic influence matrices, whose components are given by:

$$A_{\theta,w}^{ij} = \int_{0}^{1} f_i\left(\frac{z}{L}\right)\cdot g_j\left(\frac{z}{L}\right) d\left(\frac{z}{L}\right) \quad A_{\theta,\theta}^{ij} = \int_{0}^{1} f_i\left(\frac{z}{L}\right)\cdot f_j\left(\frac{z}{L}\right) d\left(\frac{z}{L}\right) \quad A_{w,w}^{ij} = \int_{0}^{1} g_i\left(\frac{z}{L}\right)\cdot g_j\left(\frac{z}{L}\right) d\left(\frac{z}{L}\right) \tag{12}$$

Note how, as torsion and flexion eigenfunctions are not necessarily otrhogonal between them, matrices $\mathbf{A}_{\theta,\mathbf{w}}$ and $\mathbf{A}_{\mathbf{w},\theta}$ could contain non-zero values in its diagonal. However, when $i \neq j$, $\frac{A_{\theta,w}^{ij}}{A_{\theta,w}^{ii}} < 1$, indicating that cross terms contribute to a lesser extent to the resulting motion.

Additionally, for values of the velocity below or arround the divergence, as the series are needed to be convergent, it should be possible to assume that $\frac{W_i}{W_{i+1}} > 1$, allowing then to neglect the terms with crossed contribution between low and high order modes. This hypothesis will be demonstrated in the following sections. Therefore, it will be possible to establish a set of equations, as follows:

$$\frac{1}{12}\cdot\rho_s\cdot c^3\cdot h\cdot L\cdot M^{\theta}_{ii}\ddot{\Theta}_i+\frac{GJ}{L}K^{\theta}_{ii}\Theta_i=\frac{1}{2}\rho_\infty V_\infty^2 c^2 L\left(A^{ii}_{\theta,w}\sum_{n=0}^{\infty}\frac{c_{m_w^{(n)}}c^{n-1}}{V_\infty^n}W_i{}^{(n)}+A^{ii}_{\theta,\theta}\sum_{n=0}^{\infty}\frac{c_{m_w^{(n)}}c^{n}}{V_\infty^n}\Theta_i{}^{(n)}\right) \tag{13}$$

$$\rho_s chLM^{w}_{ii}\ddot{W}_i+EI\cdot L^3K^{w}_{ii}W_i=\frac{1}{2}\rho_\infty V_\infty^2 cL\left(A^{ii}_{w,w}\sum_{n=0}^{\infty}\frac{c_{l_w^{(n)}}c^{n-1}}{V_\infty^n}W_i{}^{(n)}+A^{ii}_{w,\theta}\sum_{n=0}^{\infty}\frac{c_{l_w^{(n)}}c^{n}}{V_\infty^n}\Theta_i{}^{(n)}\right) \tag{14}$$

On the other hand, the equations governing the motion of an aeroelastic characteristic section can be expressed as:

$$I_{2D}\ddot{\theta}_{2D}+k_\theta\theta_{2D}=\frac{1}{2}\rho_\infty V_\infty^2 c^2\left(c_{m_0}+\sum_{n=0}^{\infty}\frac{c_{m_w^{(n)}}c^{n-1}}{V_\infty^n}w_{2D}{}^{(n)}+\sum_{n=0}^{\infty}\frac{c_{m_w^{(n)}}c^{n}}{V_\infty^n}\theta_{2D}{}^{(n)}\right) \tag{15}$$

$$m_{2D}\ddot{w}_{2D}+k_w w_{2D}=\frac{1}{2}\rho_\infty V_\infty^2 c\left(c_{l_0}+\sum_{n=0}^{\infty}\frac{c_{l_w^{(n)}}c^{n-1}}{V_\infty^n}w_{2D}{}^{(n)}+\sum_{n=0}^{\infty}\frac{c_{l_w^{(n)}}c^{n}}{V_\infty^n}\theta_{2D}{}^{(n)}\right) \tag{16}$$

In consequence, an inspection of the equations would lead to the next deduction: the 2D airfoil is capable to accurately represent the first mode of the 3D plate motion, when 2D properties of the airfoil are taken to be:

$$I_{2D}=\frac{1}{12}\rho_s c^3 h\frac{M^{\theta}_{11}}{A^{\theta}_{11}}\qquad k_\theta=\frac{GJ}{L^2}\frac{K^{\theta}_{11}}{A^{\theta}_{11}}\qquad m_{2D}=\rho_s ch\frac{M^{w}_{11}}{A^{\theta,w}_{11}}\qquad k_w=\frac{EI}{L^4}\frac{K^{w}_{11}}{A^{\theta,w}_{11}} \tag{17}$$

Therefore, dimensionally, it can be deduced how, for a given geometry, the aeroelastic response can be considered to be a function of the following non-dimensional parameters:

$$F_{2D}\left(\mathrm{Re},\mathrm{Ma},\frac{I_{2D}}{\frac{1}{2}\rho_\infty c^4},\frac{k_\theta}{\frac{1}{2}\rho_\infty V_\infty^2 c^2},\frac{m_{2D}}{\frac{1}{2}\rho_\infty c^2},\frac{k_w}{\frac{1}{2}\rho_\infty V_\infty^2},\frac{tV_\infty}{c},\frac{w_{2D}}{c},\theta_{2D}\right)=0 \tag{18}$$

With this selection of parameters, it will be, therefore, possible to reduce the complex 3D model to an equivalent 2D. Next sections will be dedicated to the application of this reduced model and its comparison with the complete three dimensional case. The characteristic parameter of the analysis is the non-dimensional torsion stiffness $k^*=\frac{k_\theta}{\frac{1}{2}\rho_\infty V_\infty^2 c^2}$. Additionally, it can be observed how the relationship between the flexural and torsional stiffness and mass are $c^2k_w/k_\theta\approx 0.183$ and $c^2m_{2D}/I_{2D}\approx 9.12$ for the case of study.

### 3.1. 3D correction for 2D model

As stated in Section 1, the actual aerodynamic coefficients of the plate can be affected by three dimensional effects. Therefore, it should be possible to correct the two-dimensional forces to obtain more accurate results.

In order to obtain the ratio between 3D and 2D coefficients, a steady CFD analysis is performed both for the 2D and 3D problem. Then, a corrective factor multiplies the section aerodynamic coefficients. However, inspection of Equation 19, which shows the equation governing the torsion of the corrected 2D system, leads to the conclusion that multiplying the aerodynamic coefficients by the corrective factor is completely analogous to divide both the 2D masses and stiffness by the same factor.

$$I_{2D_{corr}}\ddot{\theta}_{2D}+k_{\theta_{corr}}\theta_{2D}=\frac{1}{2}\rho_\infty V_\infty^2 c^2\left(c_{m_0}+\sum_{n=0}^{\infty}\frac{c_{m_w^{(n)}}c^{n-1}}{V_\infty^n}w_{2D}{}^{(n)}+\sum_{n=0}^{\infty}\frac{c_{m_w^{(n)}}c^{n}}{V_\infty^n}\theta_{2D}{}^{(n)}\right) \tag{19}$$

Where $I_{2D_{corr}}$, $k_{\theta_{corr}}$ are the corrected inertia and stiffness respectively. A similar analysis can be applied to the flexural degree of freedom in order to obtain the corrected mass and inertia as a function of the angle of attack.

$$I_{2D_{corr}} = \frac{c_m(\theta)}{C_M(\theta)} I_{2D} \qquad m_{2D_{corr}} = \frac{c_l(\theta)}{C_L(\theta)} m_{2D} \qquad k_{\theta_{corr}} = \frac{c_m(\theta)}{C_M(\theta)} k_\theta \qquad k_{w_{corr}} = \frac{c_l(\theta)}{C_L(\theta)} k_w \tag{20}$$

Where $c_l$ and $c_m$ are the 2D lift and pitching moment coefficients of the equivalent section; and $C_L$ and $C_M$ the lift and moment coefficients of the 3D plate.

# 4. Methodology

## 4.1. Numerical methodology for the resolution of the 2D case

As it was explained in Section 3, a three-dimensional flat plate can be calculated as a 2D equivalent section whose structural motion is governed by torsional and linear springs with stiffness $k_\theta$ and $k_w$, respectively, inertia, $I_{2D}$, and mass, $m_{2D}$. Figure 4, illustrates this transformation. Figure 4 (left) represents the real three dimensional model while Figure 4 (right) shows its 2D simplification.

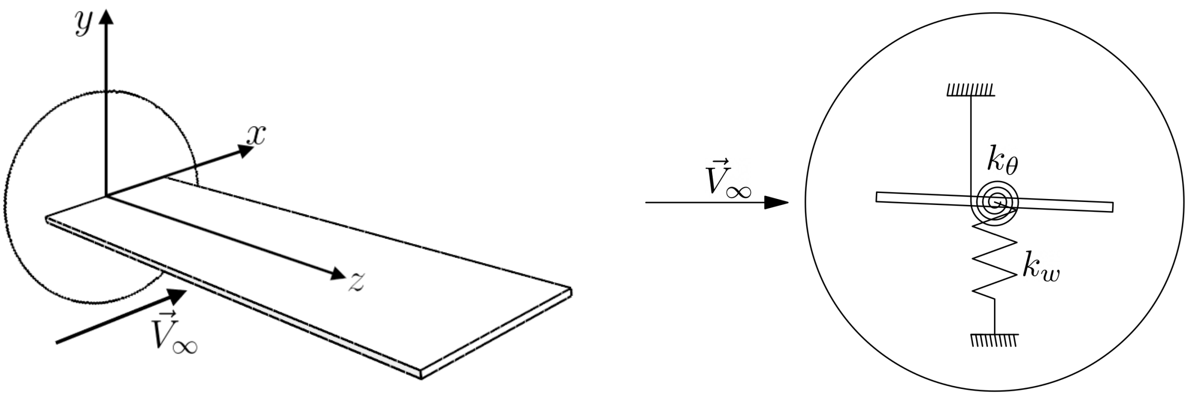


(a) 3D plate (b) 2D plate

**Figure 4:** Scheme of the three dimensional lifting flat plate (left) and its equivalent two dimensional model (right)

Equations 15 and 16 have been solved by means of the Finite Volume Method, using commercial software Simcenter STAR-CCM+®, solving the Unsteady Reynolds Average Navier Stokes (URANS) equations [33] for the fluid flow, and the rigid solid motion equations for the plate. In order to calculate flow separation under adverse pressure gradients ([34], [35]) $k-\omega$ with shear stress transport (SST) turbulence model [36] is chosen. This model varies from the $k-\omega$ turbulence model proposed by Wilcox [37] in the vicinity of the walls, to the $k-\varepsilon$ model away from them, solving the main inconveniences of both models.

For discretization, a polygonal mesh (polyhedral for 3D calculations) with second order upwind ROE FDS scheme [38] is adopted for the advection terms. The gradients are computed with a hybrid Gauss-Least Squares Method with Venkatakrishnan limiter [39]. For transient simulations, second order time discretization is used. To generate the discretized computational domain, an overset mesh methodology, which is widely used in the literature ([40], [41], [42], [43], [44]), is utilized [45].

The mesh size at the wall of the plate was taken to be approximately $\frac{\Delta x_{wall}}{c} \approx 0.004$; the mesh is gradually increasing its size from this boundary until reaching a practically uniform overset domain size of $\frac{\Delta x_{overset}}{c} \approx 0.020$, and, thus, ensuring interface similar sizes at the overset and background domains. Due to the expected importance of the wake, specially at medium-high angles of attack, the grid size is constrained to a size of $\frac{\Delta x_{wake}}{c} \approx 0.040$ at a region downstream the plate. The biggest size of the mesh at the domain is set to $\frac{\Delta x_{domain}}{c} \approx 0.200$. In order capture the effects of the wall boundary layer, a prism layer is generated near the wall, with a thickness $\frac{\Delta y}{c} = 0.075$, containing a total of 5 layers, ensuring a maximum value of $y^+ < 1$ for the most part of the wall, as will be shown later. This configuration results in a computational mesh with an approximately $5.1 \cdot 10^4$ elements. As an example, Figure 5 shows an sketch of the constructed grid.

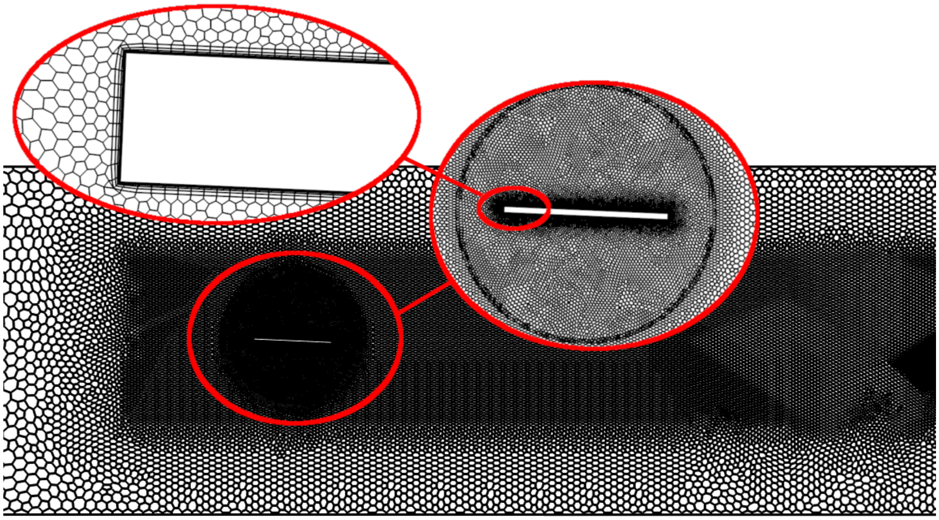

**Figure 5**: Sketch of the computational mesh (not scale) showing the different zones of refinement.

In order to check the spatial discretization, a grid independence study was performed using different cell resolutions. The study consisted on the obtainment of the aerodynamic forces and moments as a function of the steady angle of attack, as shown at Figure 6 where lift (left) and moment (right) coefficients measured at the center of the plate, are shown as a function of the angle of attack for different levels of grid resolution. It can be observed a fair agreement between all meshes for these parameters, even at angles near to stall. Similar trends are observed at the drag coefficient but, as this parameter should not be dominant on the plate motion, it is not shown. The 2D aerodynamic coefficients are defined from the 2D drag, $F'_D$, lift, $F'_L$ and moment, $M'$, measured at the center of the section, as stated by Equation 21:

$$c_d = \frac{F'_D}{\frac{1}{2}\rho_\infty V_\infty^2 c} \qquad c_l = \frac{F'_L}{\frac{1}{2}\rho_\infty V_\infty^2 c} \qquad c_m = \frac{M'}{\frac{1}{2}\rho_\infty V_\infty^2 c^2} \tag{21}$$

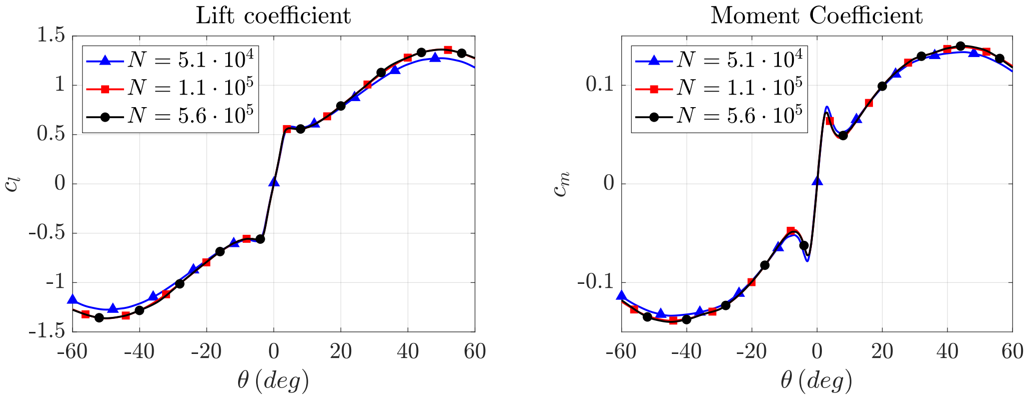


**Figure 6**: Comparison of lift (left) and moment (right) coefficients, measured at the center of the plate, for the 2D plate as a function of the angle of attack for different grid refinements

As it was previously stated, it is intended to obtain a resolution of the momentum boundary layer. In order to do this, it is necessary to ensure that the wall $y^+$ is kept in the viscous sublayer ($y^+ < 5$) for the major part of the wall. Figure 7 (left) shows the evolution of this parameter at the suction and pressure side for different values of the angle of attack. Note how $y^+ < 1$ for the whole plate. Moreover, this parameter allows to recognize how, even for the low angle of $\theta = 1$ deg a recirculation bubble appears at the suction side, extending for almost the 50 % of the length. For $\theta = 5$ deg, the recirculation is found for the whole length. These trends are confirmed by Figure 7 (right), where the distribution of the pressure coefficient ($c_p = \frac{p-p_\infty}{\frac{1}{2}\rho_\infty V_\infty^2}$) is shown for different values of the angle of attack. Note how the effects of the recirculation bubble can be inferred from the observation of an almost flat curve at the suction side of the plate.

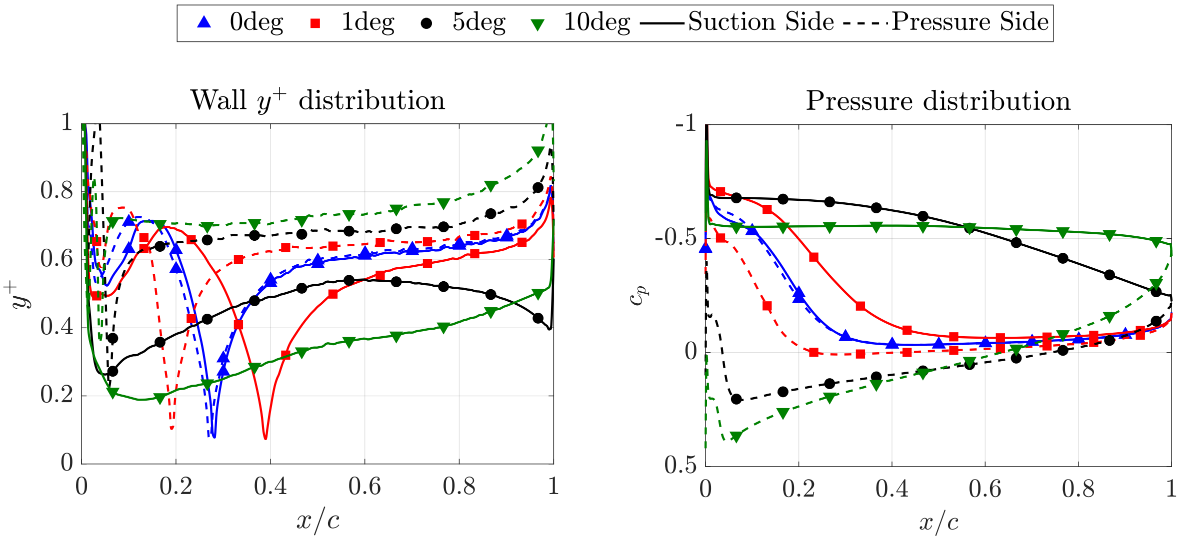


(a) $y^+$ distribution over the plate

(b) $c_p$ distribution over the plate

**Figure 7**: Distribution of wall $y^+$ (left) and pressure coefficient, $c_p$ (right) over the plate at different angles of angle of attack.

In order to correctly model unsteady effects, Courant-Lewis-Federich number $\left(\text{CFL} = \frac{\Delta t V}{\Delta x}\right)$ should be maintained to as low as possible for most part of the computational domain. For the current mesh with $N = 3.5 \cdot 10^4$ a time step of $\Delta t \cdot c/V_\infty = 1.25 \cdot 10^{-6}$ was chosen. Figure 8a shows the distribution of CFL at an arbitrary instant, for a rigid angle of attack of $\theta_0 = 2.5$ deg at conditions of $\frac{k_\theta}{\frac{1}{2}\rho_\infty V_\infty^2 c^2} = 6.44$ and $\mathrm{Re} \approx 10^5$. For the mentioned conditions the major part of the cells present a CFL lower than 2 and 90% of the volume has a CFL lower than 1.5.

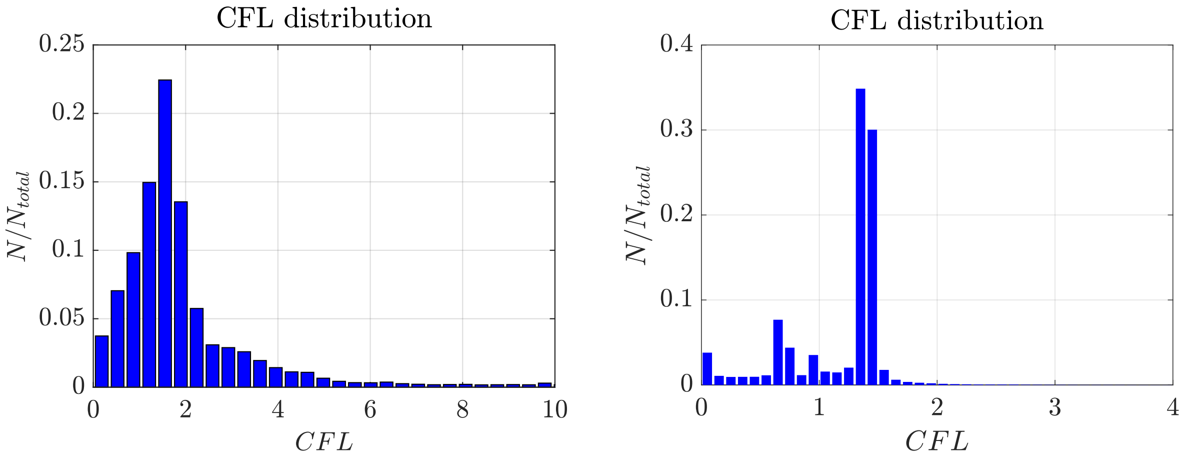


(a) 2D mesh (b) 3D mesh

**Figure 8:** CFL distribution of the mesh for the specified time step at an arbitrary instant for the 2D (left) and 3D (right) computations.

For each value of stiffness or velocity, the case is firstly initialized with a steady-rigid fluid field. This is used as the initial condition for the unsteady flexible simulation, which is iterated until steady or statistically steady conditions are reached.

## 4.2. Numerical methodology for the resolution of the 3D case

The three-dimensional case uses the Finite Volume Method for solving the URANS equations named in the previous subsection for the fluid flow and the elastic solid equations for the plate [46], [47]. To simulate the motion of the solid, an overset region is set around it, in order to ensure maintenance of the overall quality of the mesh. The plate is deformed as a consequence of the applied fluid pressure and is modeled as a flexible linear body. The overset interface can be freely deformed in accordance with the plate motion and the rest of the cells of the region are interpolated using radial basis functions (RBF) from the solid boundary displacement [48].

The mesh size had to be increased in comparison with the 2D calculations, in order to state computational requirements bounded. The cell size at the walls was set to $\frac{\Delta x_{wall}}{c} \approx 0.010$ , growing to a size of $\frac{\Delta x_{overset}}{c} \approx 0.020$ at the overset. The size at the wake was set to $\frac{\Delta x_{wake}}{c} \approx 0.040$ and the maximum size at the furthest surfaces was $\frac{\Delta x_{domain}}{c} \approx 0.400$ . With this configuration, the mesh is conformed by a total of $N \approx 5 \cdot 10^6$ elements, Figure 9 shows an image of the mesh. For the time discretization a temporal step of $\Delta t \cdot c/V_\infty = 5.00 \cdot 10^{-7}$ s is used. In addition, the time step follows the criteria for the CFL number (Figure 8b) which is lower than 1 for a 92% of the volume.

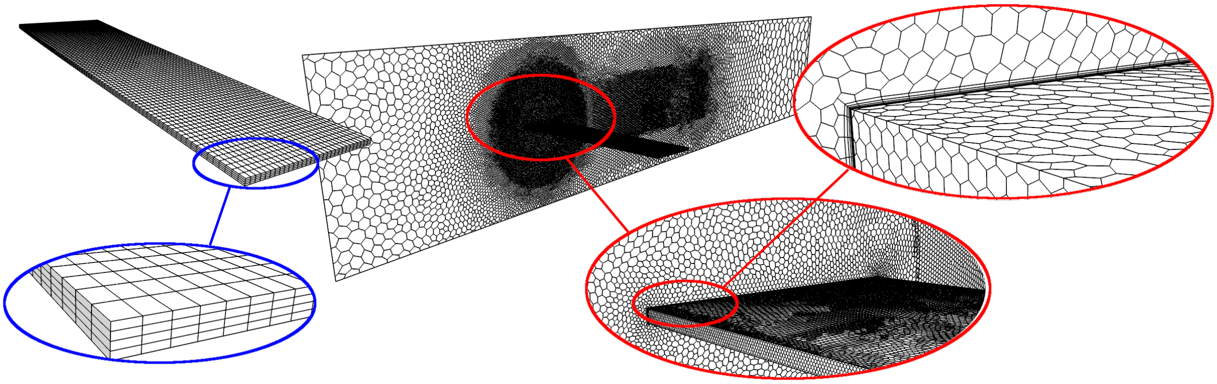

**Figure 9**: Solid mesh (left) and fluid mesh (right) of the 3D simulation. Detail on the plate and the boundary layer

In a similar way, as shown for the 2D geometry, it is necessary to ensure that the solution is not dependent on the discretization. In this sense, it was chosen to perform an spatial grid independence study based on the calculation of the stationary fluid field around the 3D plate, whose results are shown at Table 1. Observe how the discrepancies between the different simulations are minimal, ensuring grid independence of the fluid solution. The force and moment coefficients around the center of the clamped plate section are calculated in accordance with Equation 22:

$$C_D = \frac{F_D}{\frac{1}{2}\rho_\infty V_\infty^2 S_w} \qquad C_L = \frac{F_L}{\frac{1}{2}\rho_\infty V_\infty^2 S_w} \qquad C_M = \frac{M}{\frac{1}{2}\rho_\infty V_\infty^2 S_w c} \tag{22}$$

Being $S_w = L\ c$ the reference surface of the plate and $F_D$, $F_L$ and $M$ the drag, lift and moment, respectively, exerted over the plate.

**Table 1**
Comparison of the 3D force coefficients at different values of the angle of attacks for three different discretizations

| | Mesh $N = 4.7 \cdot 10^6$ | | | Mesh $N = 7.0 \cdot 10^6$ | | | Mesh $N = 15 \cdot 10^6$ | | |
|---|---|---|---|---|---|---|---|---|---|
| $\alpha$(deg) | $C_D$ | $C_L$ | $C_M$ | $C_D$ | $C_L$ | $C_M$ | $C_D$ | $C_L$ | $C_M$ |
| 0.0 | 0.0473 | 0.0000 | 0.0000 | 0.0450 | 0.0000 | 0.0000 | 0.0438 | 0.0000 | 0.0000 |
| 2.5 | 0.0555 | 0.2554 | 0.0585 | 0.0554 | 0.2554 | 0.0585 | 0.0541 | 0.2613 | 0.0602 |
| 5.0 | 0.0872 | 0.4945 | 0.0804 | 0.0867 | 0.4861 | 0.0711 | 0.0858 | 0.4826 | 0.0697 |
| 10 | 0.1551 | 0.5727 | 0.0687 | 0.1550 | 0.5725 | 0.0677 | 0.1535 | 0.5684 | 0.0659 |

Although the vibration modes of a clamped flat plate can be obtained theoretically [32], the Finite Element Method is used in order to generalize the procedures to any possible geometry and boundary conditions. The plate is discretized with elements of uniform size $\frac{\Delta x_{plate}}{c} \approx 0.035$ at the surface and a total of 4 elements through the thickness.

With these values, the eigenfrequencies and eigenvectors of the plate are calculated. It could be supposed that the discretization is good enough when the location value of the first 8 eigenfrequencies is not substantially modified when changing the mesh. Note that, if the resonance frequency, $f_i$ was expressed in terms of the Strouhal number, $\mathrm{St_i} = \frac{f_i c}{V_\infty}$, the $i^{th}$ Strouhal resonance frequency could always be expressed as a function of the non-dimensional stiffness ($k^*$) and mass ($I^* = \frac{I_{2D}}{\frac{1}{2}\rho_\infty c^4}$), in accordance with Equation 23:

$$\mathrm{St}_i = C_i \frac{L}{h}\sqrt{\frac{k^*}{I^*}} \tag{23}$$

If the constant $C_i$ is known, the vacuum resonance frequency can be calculated at any working condition. Table 2 shows the value of each of these constants for different solid mesh discretizations for the current aspect ratio of $2L/c = 7.4$. It can be observed how the result of the eigenfrequency is not noticeably affected by the number of elements chosen at each case. In consequence, the structural spatial resolution for $N = 8.5 \cdot 10^3$ elements can be considered to be accurate enough from this point of view.

**Table 2**
Comparison of the vacuum resonance frequency for two different discretizations

| $N$ | $C_1$ (bending) | $C_2$ (bending) | $C_3$ (torsional) | $C_4$ (bending) | $C_5$ (torsional) |
|---|---|---|---|---|---|
| $8.5 \cdot 10^3$ | $2.44 \cdot 10^{-4}$ | $1.52 \cdot 10^{-3}$ | $1.77 \cdot 10^{-3}$ | $4.28 \cdot 10^{-3}$ | $5.49 \cdot 10^{-3}$ |
| $5.0 \cdot 10^4$ | $2.42 \cdot 10^{-4}$ | $1.49 \cdot 10^{-3}$ | $1.73 \cdot 10^{-3}$ | $4.19 \cdot 10^{-3}$ | $5.35 \cdot 10^{-3}$ |

# 5. Results

This section presents the main results obtained during the current work. For easing its interpretability it is subdivided in two different sections: In first place, the aerodynamics of the rigid three-dimensional plate and its equivalent rigid two-dimensional characteristic section are presented, in order to quantify the corrective factor introduced at Section 3.1. Later, the deformation of the two systems is analyzed, starting with a validation of the hypothesis of neglecting high order modes and following with the capability of the two dimensional model for obtaining both the average deformation results and the beginning of instability aeroelastic zone.

## 5.1. Aerodynamic analysis

As it was previously stated, one important drawback of the reduction of dimensions is that, for a three-dimensional geometry, the aerodynamic loads are expected to vary as a function of the position in the span direction. In fact, for low values of the angle of attack, it is well known that a vortex is produced at the tip of any lifting surface, leading to an important reduction of lift compared with the pure two dimensional body. Similar effects could be observed when $\theta$ takes moderate-high values, although the effects of the tip are slightly different. Moreover, the center of pressure is moved and the aerodynamic moment is also modified. To visualize these effects, in Figure 10, the evolution of the force coefficients of the 3D plate with the depth coordinate are presented for two low and one moderate angles of attack. This figure shows how, as explained before, the aerodynamic correction of Section 3.1 should be applied to reproduce the effects of 3D aerodynamics. Note how integration about the $z$ axis would allow to obtain the global aerodynamic coefficient of the plate. Figure 10a shows the distribution of lift coefficient. Observe how near the clamping ($z/L = 0$), the force can be considered to be approximately constant, decreasing, for low values of angle of attack when reaching coordinates near to the tip ($z/L \approx 1$). For moderate-high $\theta$, the three-dimensional effects of the plate and the influence of the channel's walls produce an increase in lift close to the tip. Similar effects can be observed for the pitching moment, which is shown at Figure 10b.

Three-dimensional effects can also be illustrated by means of Figure 11, which shows the streamlines of the wall shear stress over the plate, colored by the value of the pressure coefficient, for different $\theta$. These lines indicate the direction of the air over the plate and can be easily used for identifying different flow patterns, namely the existence of a recirculation bubble beginning at the leading edge of the suction side even for very low $\theta$. Note how, for the case of $\theta = 2\,\mathrm{deg}$, this bubble is shorter at the tip and its size tends to increase when reaching the $z/L = 0$ position, where it occupies approximately the 25 % of the chord. The recirculation bubble grows when increasing the angle of attack (for instance, at $\theta = 4\,\mathrm{deg}$ it occupies almost 80 % of the chord) until its length correspond to the whole chord for high angles of attack.

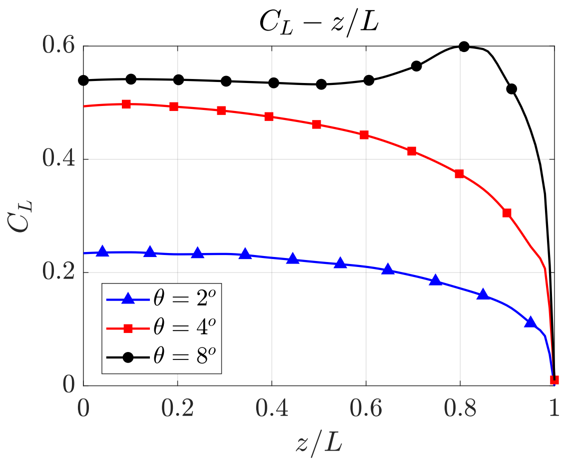


(a) Lift distribution

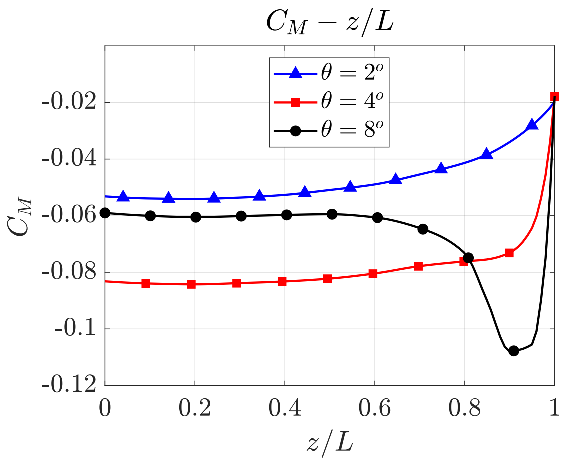


(b) Moment distribution

**Figure 10:** Distribution of lift force (left) and pitching (right) moment along the span measured at the center of the chord.

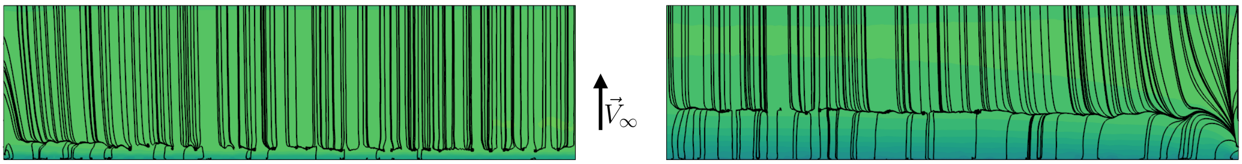


(a) Pressure side - $\theta = 2°$ (b) Suction side - $\theta = 2°$

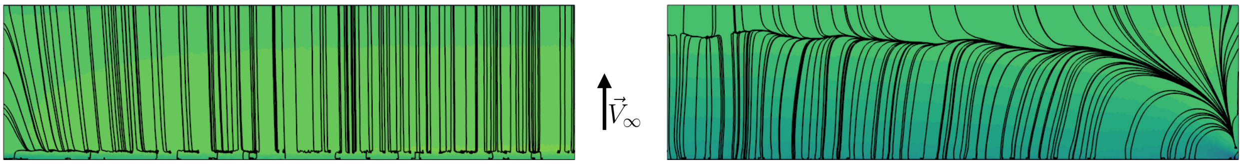


(c) Pressure side - $\theta = 4°$ (d) Suction side - $\theta = 4°$

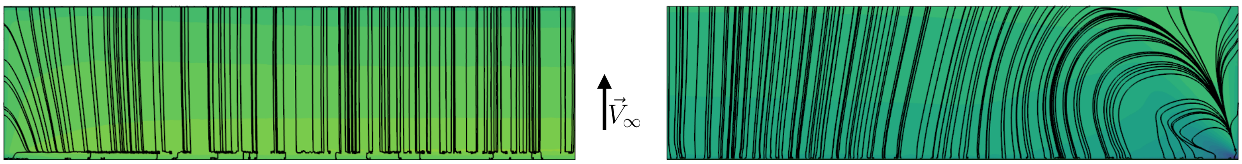


(e) Pressure side - $\theta = 8°$ (f) Suction side - $\theta = 8°$

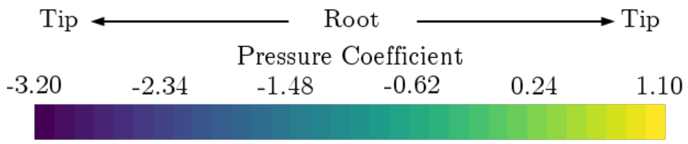


**Figure 11:** Pressure coefficient distribution and wall shear stresses at the pressure side (left) and suction side (right) for different values of angle of attack

Figure 12 might also be useful for visualization of these effects. Here, streamlines passing near to the plate's tip are shown both the perfectly rigid configuration (left) and at an arbitrary time step of the statistically stationary fully coupled solution, corresponding to a non-dimensional stiffness parameter of $k^* = 6.44$. As expected, similar fluid patterns can be inferred from the stream lines of both figures. Additionally, turbulence kinetic energy, $k$, is visualized, non-dimensionalized with the free stream velocity.

Streamlines show the vortex produced at the tip of the plate. A high turbulence kinetic energy zone starts after the sharp edge of the plate and continues downwards. The higher value of the turbulent kinetic energy is obtained in the recirculation bubble of the suction side, near to the shear layer. Then the kinetic energy is diffused downwards and its value is decreased until it is dissipated.

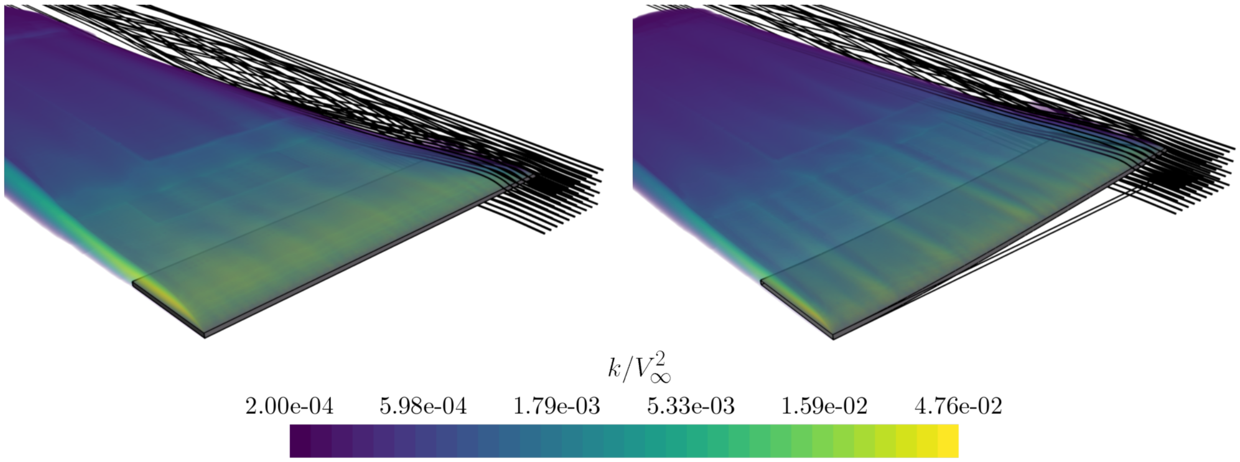


**Figure 12:** 3D effects on the flat plate with $\theta_0 = 2.5$ deg. Figure shows the solution for rigid plate (left, $k^* \to \infty$) and for an arbitrary time step corresponding with the simulations of a flexible plate of $k^* = 6.44$

Therefore, in order to obtain an accurate two-dimensional aeroelastic model, applicable to a wide range of angles of attack and non-dimensional stiffness, quantification of these effects over the global force and moment coefficients needs to be performed. Figure 13 illustrates the variation of the lift coefficient. The global lift coefficient ($3\mathrm{D}_{\mathrm{global}}$) is also shown. Note how, as expected, force coefficient near the root is similar to the two-dimensional calculation, although slightly minored. However, the value near the tip is far different from the 2D case. A correction for the lift coefficient is proposed in Figure 13b. This global correction uses the coefficient value of the 3D simulation to correct 2D results. Similar effects are observed for the pitching moment, shown in Figure 14.

In Figures 13 and 14, it is possible to appreciate how, for low $\theta$ the lift and moment in the 2D problem are higher than in the 3D simulation. For moderate to high values of the angle of attack, two-dimensional plate stalls while in the value of $C_M$ continues increasing. Therefore, the correction applied to the 2D problem must decrease the value of the coefficients in the first zone and after a stall angle of attack, the coefficient must be amplified.

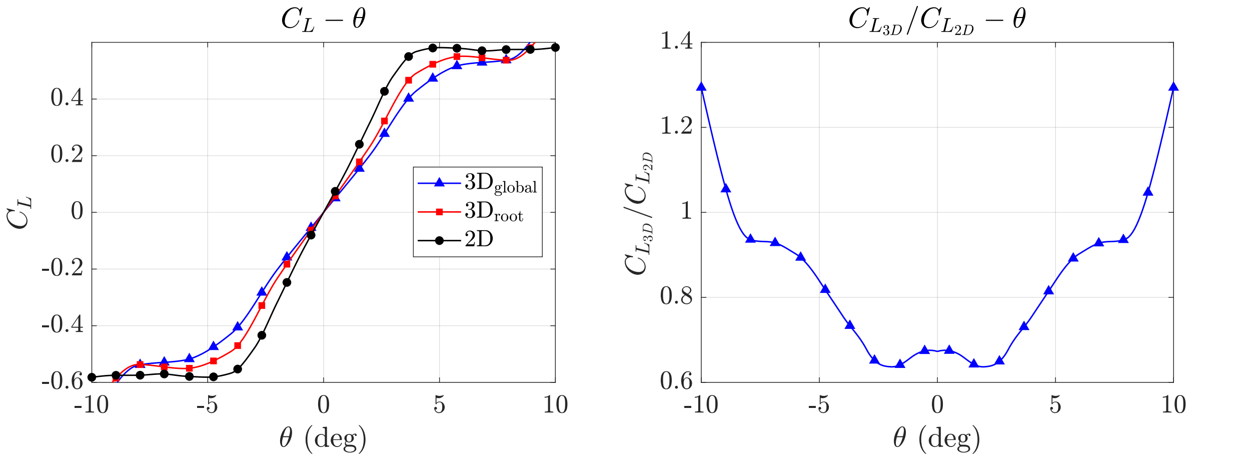


(a) Lift coefficient

(b) Lift correction

**Figure 13:** Lift coefficient for 2D section, root section and global 3D plate (left) and scaling coefficient for the lift force (right).

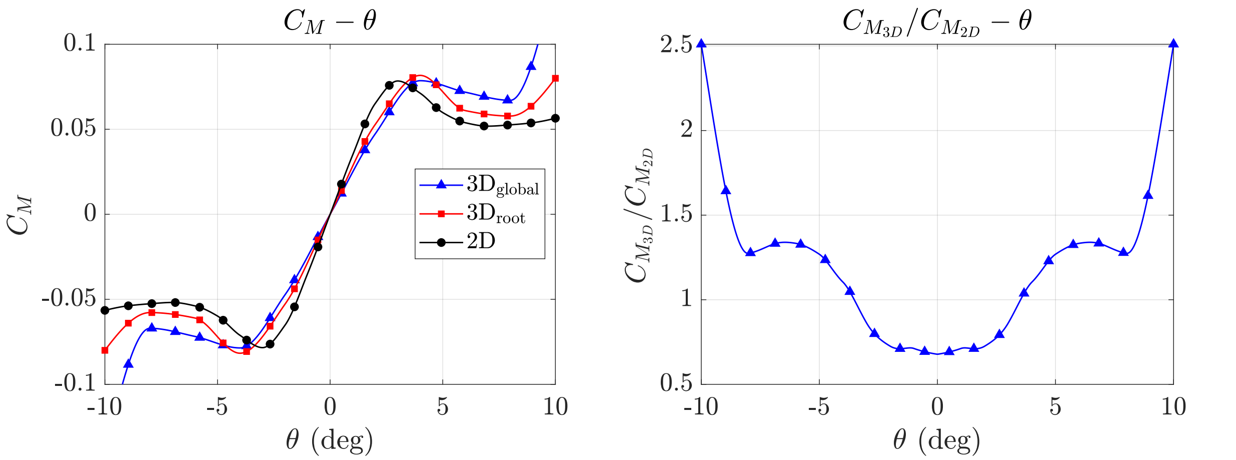


(a) Pitch moment coefficient

(b) Pitch moment correction

**Figure 14:** Pitch moment coefficient for 2D section, root section and global 3D plate (left) and scaling coefficient for the pitch moment (right).

## 5.2. Deformation results and instability analysis

The methodology derived during Section 3 took as hypothesis that only first modes of torsion and bending are dominant for quantifying the aeroelastic features of the system for values of the non-dimensional stiffness above aeroelastic instability. In order to examine the accuracy of neglecting high order modes, the shape of the deformed structure is compared with the modal deformation shapes, similarly as performed at [23]. Figure 15 shows the modal contribution for bending (left) and torsion (right) for the 4 first modes. From this figure, it can be inferred how the first mode is dominant in both bending and torsion, with a modal factor contribution at least two orders of magnitude greater than the participation of higher order modes. Slight differences are observed between the first mode and the actual deformed shape. In consequence, for practical purposes, and given the substantial simplification in terms of computational cost, the hypothesis of neglecting high order modes can be considered to be accurate enough.

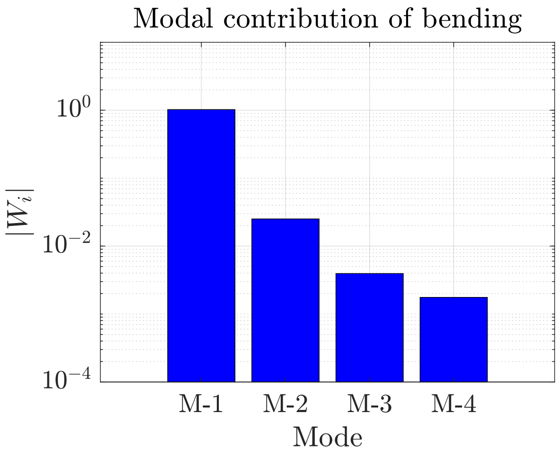


(a) Bending modal contribution

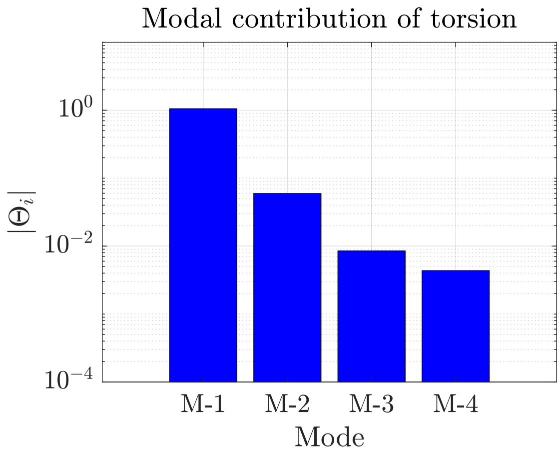


(b) Torsional modal contribution

**Figure 15:** Modal contribution for the flexural and the torsional deformations for a reference plate with $k^* = 21$

Once the contribution of the high order modes has been analyzed and shown to be of negligible importance in the computation of deformation, it is possible to establish that the structural equivalence between the 2D and 3D models can be applied for evaluating the fully coupled problem. Next, the capabilities of both models will be analyzed. Figure 16a and 16b show the time average torsion and bending, respectively, predicted by the 3D and 2D (with aerodynamic corrections) models when a statistically stationary state is reached. Some points of this curve are highlighted, as their time history will be discussed later. The gray zone represents the values of $k^*$ at which the slope of the curves becomes significantly high, which could be used as an indicator for predicting aeroelastic instabilities. Note the high capability of the 2D model for predicting the same results than the 3D for average torsion, even when not considering any kind of three dimensional effects for the 2D aerodynamic evaluation (red lines). However, this non-corrected model tends to overestimate the value of the average bending, which is in accordance with the already mentioned overestimation of the force coefficient of the 2D model.

The equivalence of the 2D and 3D models can be improved by the application of a three-dimensional aerodynamic correction. Note how, when applying a corrective factor accounting for the global coefficients of the plate (black lines), both prediction of torsion and bending obtained by the 2D and 3D models show a fair agreement.

Finally, note how the beginning of an aeroelastic instability could be identified by the observation of a zone of the curves at which the slope of both the average torsion and bending is abruptly increased, approximately for the same value of $k^* \approx 5.5$. As it will be shown later, this instability can be attributed to a stall flutter phenomenon, characterized by an oscillatory motion whose amplitude is constantly amplified with time. This phenomenon should not be confused with the classical linear flutter, as mechanisms of this last are completely different. In fact, classical linear flutter consists on a coupling between torsional and bending modes which can even be predicted ignoring aerodynamic non-linearities. Moreover in cases at which the center of gravity of the section and its elastic axis are coincident (as the current case) linear flutter is expected not to occur.

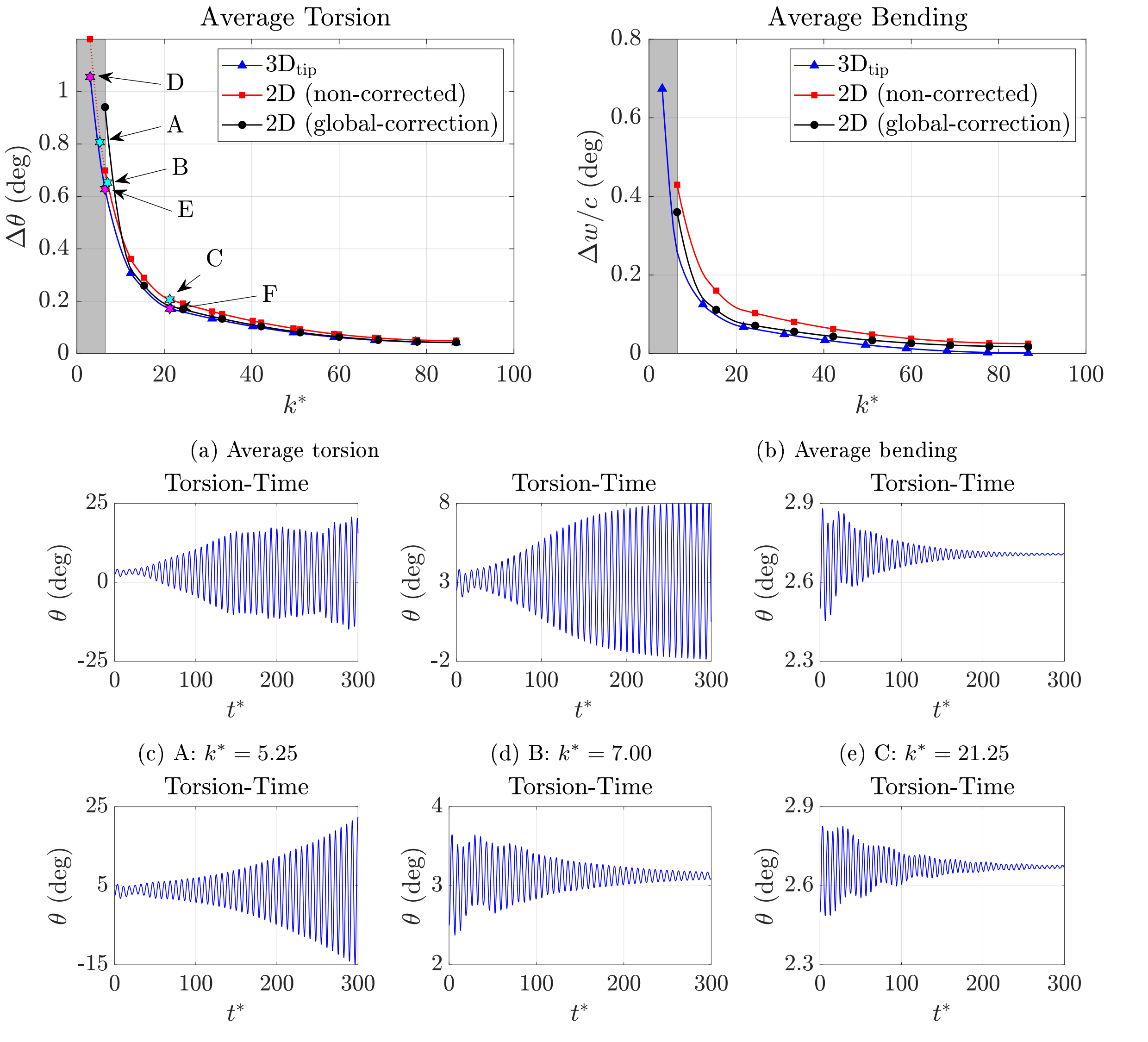


(a) Average torsion

(b) Average bending

(c) A: $k^* = 5.25$

(d) B: $k^* = 7.00$

(e) C: $k^* = 21.25$

(f) D: $k^* = 3.00$

(g) E: $k^* = 6.44$

(h) F: $k^* = 21.25$

**Figure 16**: Top: Average deformation for the non-dimensional stiffness 16a and 16b. The shaded area shows the uncertainty limit of the 2D derived section. Bottom: Temporal evolution of the pitch respect a non-dimensional time $\left(t^* = \frac{tv_\infty}{c}\sqrt{\frac{k^*}{I^*}}\right)$ for 2D simulation cases A, B and C [★] (16c 16d and 16e) and 3D simulations D, E and F [✶] (16f 16g and 16h).

The analysis of the time evolution of 2D and 3D models can be considered to be also of interest and, therefore, they will be discussed next, using the unsteady responses shown at Figures 16c-16h. Here, time is nondimensionlized as $\left(t^* = \frac{tv_\infty}{c}\sqrt{\frac{k^*}{I^*}}\right)$ in order to ease comparison between different $k^*$. Cases C (Figure 16e) and F (Figure 16h) correspond to the evolution of the 2D and 3D computations, respectively, for a relatively high value of $k^*$. Here, it can be observed how the damping introduced by the aerodynamic forces is high enough to ensure that, at a sufficiently long time, the oscillations of the system are minimal, and a steady response is reached.

When the value of $k^*$ is lower, the aerodynamic damping is decreased and, therefore, the oscillations of the system are not easily suppressed. In fact, when reaching the limit of instability, represented by the Case B (Figure 16d) for the 2D section, a stable Limit Cycle Oscillation (LCO) is observed. For this value of $k^*$

LCO is not already reached for the 3D simulation, case E (Figure 16g).

Similar trends can be observed analyzing values of $k^*$ lying inside the stall flutter aeroelastic instability zone, corresponding to Cases A (Figure 16c) and D (Figure 16f). Here, the aerodynamic damping becomes zero, or even negative and, as a result, an unstable oscillation is found, predicting the 2D calculation a much more abrupt response than the 3D case. Both cases present a similar unstable oscillatory evolution, which can be attributed to a stall flutter phenomenon.

The Limit Cycle Oscillation can be further discussed by means of Figure 17. Here, the curves of $c_l$ vs $\theta$ and the phase diagram are shown for the 2D calculation for a case just after (Case A) and just before (Case B) the instability region. Note how, at Figure 17d, for high values of time, a stable cycle can be identified, while the amplitude of the oscillation represented at Figure 17c is monotonically increased. Similar conclusions could be extracted from Figures 17a and 17b where, additionally, the high nonlinearities of the current calculations can be observed, showing a loop whose shape is significantly different to those results in the literature covering only the linear regime of angle of attack [49], [50].

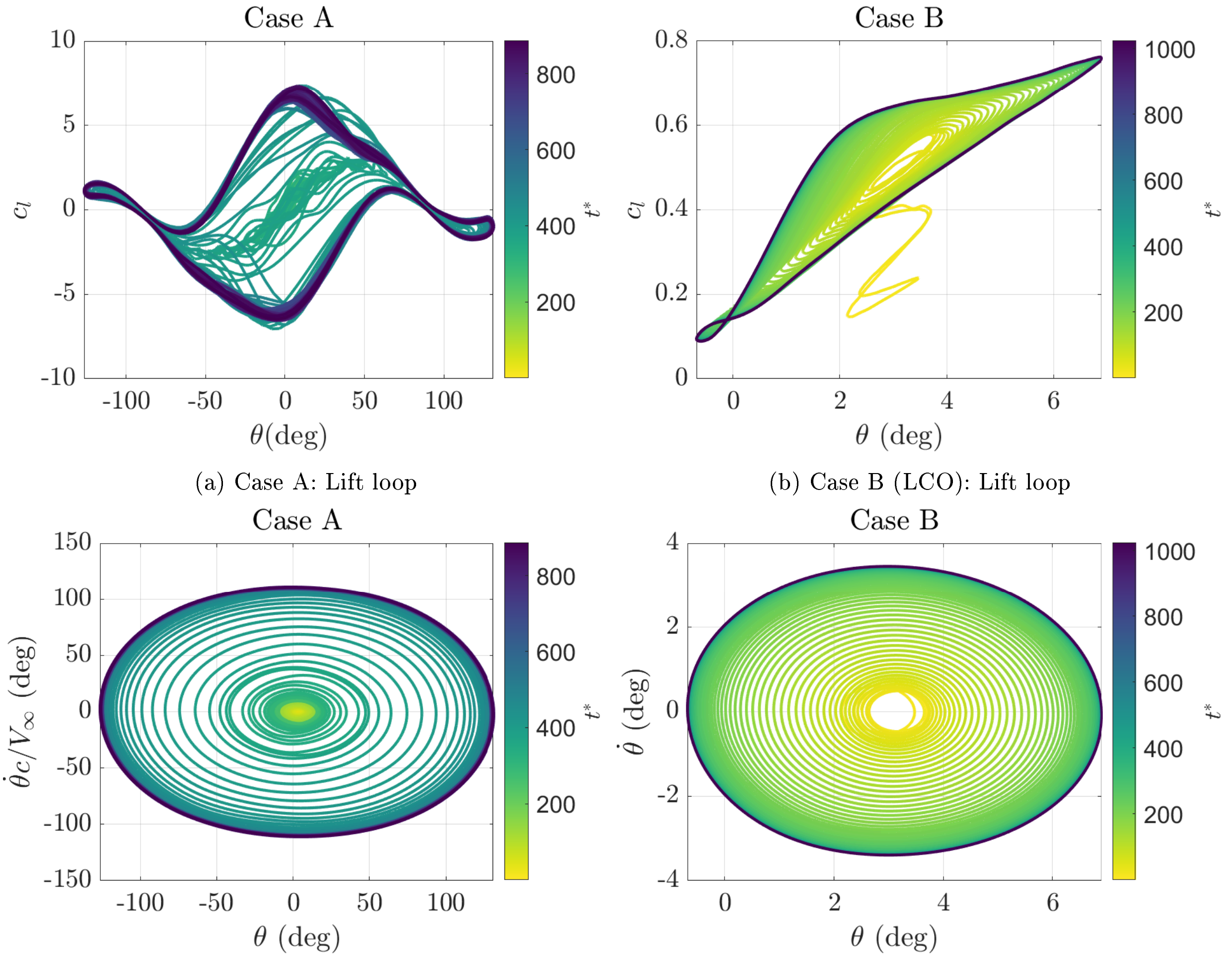


(a) Case A: Lift loop

(b) Case B (LCO): Lift loop

(c) Case A: Phase diagram

(d) Case B (LCO): Phase diagram

**Figure 17:** Aerodynamic hysteresis loop of the aeroelastic 2D simulation for flutter conditions (left) and LCO (right).

## 6. Conclusions

A methodology for obtaining an equivalent two-dimensional section from a three dimensional arbitrary structure has been presented during this work. This procedure allows modeling the main aeroelastic features of the 3D system and it is capable of accounting for aerodynamic non-linearities at arbitrary sections. The equivalent model has been shown not to be of straightforward derivation, in accordance with the literature. The main advantage of the proposed methodology is the reduction, by orders of magnitude, of the computational resources for a similar level of accuracy.

The methodology has been tested for a flat cantilevered plate inside an aerodynamic channel. Along the paper, a comparison between the 3D simulation and the equivalent 2D problem has been performed, obtaining low differences between the simplified section and the 3D case. As the 2D equivalent problem is representative of a 3D structure for most of the operation range, the procedure and methodology would allow to simulate arbitrary sections of arbitrary complex beams accounting for highly non-linear fluid dynamics effects. Relative to the aerodynamics, the wind loads calculated in the 2D simulation do not directly account for purely three-dimensional effects as tip vortex. This work, additionally, proposes and tests a corrective factor for the aerodynamic coefficients in order to obtain more accurate values of the aeroelastic deformations of the system. On the one hand, the non-corrected simulation gives good accuracy for the calculation of the pitching angle, but a slight overprediciton of bending comparing with the three-dimensional results. On the other hand, the accuracy of these predictions has been shown to be substantially improved when applying a correction accounting for the total force and moment coefficients acting over the three-dimensional rigid plate. The main important advantages of this simplified methodology can be listed next:

- Although important simplifications have been assumed during the derivation of the equivalent model, it allows to obtain accurate deformation results, implying reduction on the computational cost by orders of magnitude respect to the 3D simulation.
- The aerodynamics of the reduced bi-dimensional model can be considered to be fully non-linear, given that the hypothesis listed during its derivation could be assumed to be valid.
- Therefore, the model should be useful for relatively quick estimations of aeroelastic linear instabilities, such as flutter or divergence. Also it could be used for the estimation of non linear instabilities/phenomena such as stall flutter.

The main hypothesis of the equivalent 2D derivation have been discussed, as well as their range of applicability, showing how, even with the important simplifications which were assumed during the derivation (the coupling between low and high order modes is neglected, the differences of the total pitching angle between tip and root are bounded...) the two-dimensional simplified geometry is capable to provide with the same aeroelastic phenomena than the three dimensional plate, for the studied range of application. Therefore, the current methodology can be applied for the study of non-linear aeroelastic systems for high and medium values of the non dimensional stiffness, showing a high capacity for predicting the same deformations and instabilities zones of its equivalent 3D cases.

## 7. Acknowledges

This project was partially supported by the Spanish company "Axial Structural Solutions" in the benchmark of a collaboration project entitled "Analysis of solar plates stability". In addition, the manuscript have been partially funded by Spanish Ministry of Science, Innovation and University through the University Faculty Training (FPU) program with reference FPU19/02201.

## Symbols

| | |
|---|---|
| $\Delta\theta$ | Torsional motion |
| $\Delta w$ | Flexural motion |
| $\Delta x_{domain}$ | Largest grid size on the domain |
| $\Delta x_{overset}$ | Grid size on the overset region |
| $\Delta x_{plate}$ | Grid size on the plate |
| $\Delta x_{wake}$ | Grid size on the wake |
| $\Delta x_{wall}$ | Grid size on the walls |
| $\delta\theta$ | Pitching angle differential |
| $\delta\mathcal{W}$ | Virtual work derivative |
| $\delta w$ | Plunge differential |
| $\epsilon$ | Turbulent dissipation |
| $\vec{\Theta}$ | Vector of torsional modes amplitude |
| $\Theta_i(t)$ | Amplitude associated with torsional modes |
| $\theta_0$ | Initial pitch angle of the plate |
| $\theta_{2D}$ | Pitching angle of the 2D section |
| $\mu_\infty$ | Free stream viscosity |
| $\nu$ | Poisson coefficient |
| $\rho_\infty$ | Free stream density |
| $\rho_s$ | Solid density |
| $\omega$ | Turbulent dissipation rate |
| $\mathbf{A}_{\theta,\theta}$, $\mathbf{A}_{\theta,w}$, $\mathbf{A}_{w,\theta}$, $\mathbf{A}_{w,w}$ | Aerodynamic influence matrix |
| $a_\infty$ | Free stream speed of sound |
| $AR$ | Aspect ratio |
| $C_D$ | 3D drag coefficient |
| $C_i$ | Vacuum resonance frequency |
| $C_L$ | 3D lift coefficient |
| $C_M$ | 3D pitch moment coefficient |
| $c$ | Chord of the plate |
| $c_d$ | 2D drag coefficient |
| $c_l$ | 2D lift coefficient |
| $c_{l_\theta^{(n)}}$ | 2D lift coefficient n derivative respect to the pitch angle |
| $c_{l_w^{(n)}}$ | 2D lift coefficient n derivative respect to the vertical position |
| $c_m$ | 2D pitch moment coefficient |
| $c_{m_\theta^{(n)}}$ | 2D pitch moment coefficient n derivative respect to the pitch angle |
| $c_{m_w^{(n)}}$ | 2D pitch moment coefficient n derivative respect to the vertical position |
| CFL | Courant-Friedrichs-Levy number |
| $d\Omega$ | Differential of the volume |
| $E$ | Young's modulus |
| $F_D$ | 3D drag force |
| $F'_D$ | 2D drag force |
| $F_L$ | 3D lift force |
| $F'_L$ | 2D lift force |
| $f_i$ | Torsional eigenfunction |

| | |
|---|---|
| $G$ | Transversal elastic modulus |
| $g_i$ | Bending eigenfunction |
| $H$ | Section of the wind tunnel |
| $h$ | Thickness of the plate |
| $I$ | Second moment of area of the section |
| $I^*$ | Non-dimensional inertia of the cross section of the plate |
| $I_{2D}$ | 2D inertia of the plate |
| $I_{2D_{corr}}$ | 2D inertia of the plate corrected with 3D aerodynamics |
| $J$ | Polar moment of inertia |
| $\mathbf{K}_\theta$ | Stiffness matrix of the torsional modes |
| $\mathbf{K}_w$ | Stiffness matrix of the flexural modes |
| $k$ | Turbulent kinetic energy |
| $k^*$ | Characteristic non-dimensional stiffness of the plate |
| $k_\theta$ | 2D torsional stiffness |
| $k_{\theta_{corr}}$ | 2D torsional stiffness corrected with 3D aerodynamics |
| $k_w$ | 2D flexural stiffness |
| $k_{w_{corr}}$ | 2D flexural stiffness corrected with 3D aerodynamics |
| $L$ | Span of the plate |
| $L_d$ | Downwind distance domain |
| $L_u$ | Upwind distance domain |
| $M$ | 3D pitch moment |
| $M'$ | 2D pitch moment |
| $\mathbf{M}_\theta$ | Mass matrix of the torsional modes |
| $\mathbf{M}_w$ | Mass matrix of the flexural modes |
| $m_{2D}$ | 2D mass of the plate |
| $m_{2D_{corr}}$ | 2D mass of the plate corrected with 3D aerodynamics |
| Ma | Mach number |
| $N$ | Number of elements |
| $Q_{q_j}$ | Generalized forces |
| $q_j$ | Generalized coordinate of the plate |
| $S_w$ | Reference surface of the plate |
| St | Strouhal number |
| $T$ | Kinetic energy of the plate |
| $t$ | Time |
| $t^*$ | Non-dimensional time |
| $U$ | Potential energy of the plate |
| Re | Reynolds number |
| $V_\infty$ | Free stream velocity |
| $\vec{W}$ | Vector of flexural modes amplitude |
| $W_i(t)$ | Amplitude associated with flexural modes |
| $w_0$ | Initial vertical position of the plate |
| $w_{2D}$ | Plunge of the 2D section |
| $x$ | Position coordinate |
| $y$ | Position coordinate |
| $y_p$ | Vertical displacement of a point over the plate |
| $z$ | Position coordinate |

# References

[1] G. Rogers, J. Kristof, Reducing operational and product costs through environmental accounting, Environmental Quality Management 12 (2003) 17–42.

[2] B. Briseghella, L. Fenu, C. Lan, E. Mazzarolo, T. Zordan, Application of topological optimization to bridge design, Journal of Bridge Engineering 18 (2013) 790–800.

[3] C. Ledermann, P. Ermanni, R. Kelm, Dynamic cad objects for structural optimization in preliminary aircraft design, Aerospace Science and Technology 10 (2006) 601–610.

[4] D. K. Koli, G. Agnihotri, R. Purohit, Advanced aluminium matrix composites: The critical need of automotive and aerospace engineering fields, Materials Today: Proceedings 2 (2015) 3032–3041.

[5] M. Blair, T. A. Weisshaar, Swept composite wing aeroelastic divergence experiments, Journal of Aircraft 19 (1982) 1019–1024.

[6] L. Librescu, S. Thangjitham, Analytical studies on static aeroelastic behavior of forward-swept composite wing structures, Journal of Aircraft 28 (1991) 151–157.

[7] J. P. Thomas, E. H. Dowell, K. C. Hall, Nonlinear inviscid aerodynamic effects on transonic divergence, flutter, and limit-cycle oscillations, AIAA journal 40 (2002) 638–646.

[8] L. Sanches, T. A. Guimaraes, F. D. Marques, Aeroelastic tailoring of nonlinear typical section using the method of multiple scales to predict post-flutter stable lcos, Aerospace Science and Technology 90 (2019) 157–168.

[9] T. Zhou, E. Dowell, S. S. Feng, Computational investigation of wind tunnel wall effects on buffeting flow and lock-in for an airfoil at high angle of attack, Aerospace Science and Technology 95 (2019) 105492.

[10] R. Camussi, A. Di Marco, C. Stoica, M. Bernardini, F. Stella, F. De Gregorio, D. Barbagallo, Wind tunnel measurements of the surface pressure fluctuations on the new vega-c space launcher, Aerospace Science and Technology (2020) 105772.

[11] J. Sodja, F. Roizner, R. De Breuker, M. Karpel, Experimental characterisation of flutter and divergence of 2d wing section with stabilised response, Aerospace Science and Technology 78 (2018) 542–552.

[12] E. Camilo, F. D. Marques, J. L. F. Azevedo, Hopf bifurcation analysis of typical sections with structural nonlinearities in transonic flow, Aerospace Science and Technology 30 (2013) 163–174.

[13] E. Dowell, A Modern Course in Aeroelasticity, Springer, 2015.

[14] C. Peng, H. Jinglong, Prediction of flutter characteristics for a transport wing with wingtip device, Aerospace Science and Technology 23 (2012) 461–468.

[15] N. Tsushima, W. Su, Flutter suppression for highly flexible wings using passive and active piezoelectric effects, Aerospace Science and Technology 65 (2017) 78–89.

[16] H. J. Kwon, D. H. Kim, I. Lee, Frequency and time domain flutter computations of a wing with oscillating control surface including shock interference effects, Aerospace Science and Technology 8 (2004) 519–532.

[17] B. Wu, X. Chen, Q. Wang, H. Liao, J. Dong, Characterization of vibration amplitude of nonlinear bridge flutter from section model test to full bridge estimation, Journal of Wind Engineering & Industrial Aerodynamics 197 (2020) 104048.

[18] B. Wu, Q. Wang, H. Liao, Y. Li, M. Li, Flutter derivatives of a flat plate section and analysis of flutter instability at various wind angles of attack, Journal of Wind Engineering & Industrial Aerodynamics 196 (2020) 104046.

[19] H. Tang, K. Shum, Y. Li, Investigation of flutter performance of a twin-box bridge girder at large angles of attack, Journal of Wind Engineering & Industrial Aerodynamics 186 (2019) 192–203.

[20] Z. J. Taylor, M. T. Browne, Hybrid pressure integration and buffeting analysis for multi-row wing loading in an array of single-axis trackers, Journal of Wind Engineering & Industrial Aerodynamics 197 (2020) 104056.

[21] A. Schellenberg, J. Maffei, K. Tellen, R. Ward, Structural analysis and application of wind loads to solar arrays, Journal of Wind Engineering & Industrial Aerodynamics 123 (2013) 261–272.

[22] C. kwon Kang, H. Aono, Y. S. Baik, L. P. Bernal, W. Shyy, Fluid dynnamics of pitching and plunging flat plate at intermediate reynolds numbers, AIAA Journal 51 (2013).

[23] A. Torregrosa, A. Gil, P. Quintero, A. Ammirati, H. Denayer, W. Desmet, Prediction of flow induced vibration of a flat plate located after a bluff wall mounted obstacle, Journal of Wind Engineering & Industrial Aerodynamics 190 (2019) 23–39.

[24] K. O. Gralund, M. V. Ol, L. P. Bernal, Unsteady pitching flat plates, Journal of Fluid Mechanics 733 (2013).

[25] M. Savage, G. Larose, An experimental study of the aerodynamic influence of a pair of winglets on a flat plate model, Journal of Wind Engineering and Industrial Aerodynamics 91 (2003) 113–126.

[26] A. Attaran, D. Majid, S. Basri, A. Mohd Rafie, E. Abdullah, Structural optimization of an aeroelastically tailored composite flat plate made of woven fiberglass/epoxy, Aerospace Science and Technology 15 (2011) 393–401.

[27] C. M. Jubayer, H. Hangan, A numerical approach to the investigation of wind loading on an array of ground mounted solar photovoltaic (pv) panels, Journal of Wind Engineering and Industrial Aerodynamics 153 (2016) 60–70.

[28] G. P. Reina, G. De Stefano, Computational evaluation of wind loads on sun-tracking ground-mounted photovoltaic panel arrays, Journal of Wind Engineering and Industrial Aerodynamics 170 (2017) 283–293.

[29] G. L. Larose, F. M. Livesey, Performance of streamlined bridge decks in relation to the aerodynamics of a flat plate, Journal of Wind Engineering and Industrial Aerodynamics 69-71 (1997) 851–860.

[30] A. Rezaeiha, I. Kalkman, B. Blocken, Cfd simulation of a vertical axis wind turbine operating at a moderatetip speed ratio: Guidelines for minimum domain size and azimuthalincrement, Renewable Energy 107 (2017) 373–385.

[31] H. Goldstein, C. Poole, J. Safko, Classical Mechanics, Addison Wesley, 2000.

[32] R. D. Blevins, Formulas for natural frequency and mode shape, Van Nostrand Reinhold Company, 1979.

[33] S. Pope, Turbulent Flows, Cambridge University Press, 2009.

[34] R. Gavasane, P. Pai, V. Kumar, Numerical simulation of pitching and plunging motion of flat plate using oversetmeshes, Symposium on Applied Aerodynamics and Design of Aerospace Vehicle (SAROD 2013), 2013.

[35] J. Morgado, R. Vizinho, M. Silvestre, J. Páscoa, Xfoil vs cfd performance predictions for high lift low reynolds number airfoils, Aerospace Science and Technology 75 (2016) 207–214.

[36] F. Menter, Zonal two-equation $k-\omega$ turbulence model for aerodynamic flows, AIAA 93 (1986) 93–2906.

[37] D. Wilcox, Multiscale model for turbulent flows, Proceedings of the 24th AIAA Aerospace Science Meeting 24 (1986) 1311–1320.

[38] P. Roe, Approximate riemann solvers, parameter vectors, and difference schemes, Journal of Computational Physics 135 (1981) 250–258.

[39] V. Venkatakrishnan, On the convergence of limiters and convergence to steady state solutions, AIAA-93-0880 (1995).

[40] T. T. Tran, D. Kim, The platform pitching motion of floating offshore wind turbine: A preliminary unsteady aerodynamic analysis, Journal of Wind Engineering & Industrial Aerodynamics 142 (2015) 65–81.

[41] T. T. Tran, D. Kim, A cfd study into the influence of unsteady aerodynamic interference on wind turbine surge motion, Renewable energy 90 (2016) 204–228.

[42] T. T. Tran, D. Kim, J. Song, Computational fluid dynamic analysis of a floating offshore wind turbine experiencing platform pitching motion, Energies 7 (2014) 5011–5026.

[43] B. Dose, H. Rahimi, B. Stoevesandt, J. Peinke, Fluid-structure coupled investigations of the nrel 5mw wind turbine for two downwind configurations, Renewable energy 146 (2020) 1113–1123.

[44] A. Marouf, N. Simiriotis, J. To, Y. Bmegaptche, Y. Hoarau, M. Braza, Ddes and oes simulations of a morphing airbus a320 wing and flap in different scales at high reynolds, Progress in Hybrid RANS-LES Modelling (2020) 249–258.

[45] H. Hadzic, Development and application of finite volume method for the computation of flows around moving bodies on unstructure, overlapping grids (2005).

[46] O. Zienkiewicz, R. Taylor, D. Fox, The Finite Element Method for Solid and Structural Mechanics, Elsevier, 2014.

[47] A. Torregrosa, A. Gil, L. García-Cuevas, P. Quintero, F. Denia, Prediction of the transmission loss in a flexible chamber, Journal of Fluids and Structures 82 (2018) 134–153.

[48] S. Lee, G. Wolberg, S. Y. Shin, Scattered data interpolation with multilevel b-splines, IEEE Transactions on Visualization and Computer Graphics 3 (1997).

[49] A. Hassan, S. Mohammad-Reza, M. Mohammand-Javad, Transitional boundary layer study over an airfoil in combined pitch-plunge motions, Aerospace Science and Technology 98 (2020) 105694.

[50] D. Williams, F. Reissner, D. Greenblatt, H. Muller-Vahl, C. Strangfeld, Modeling lift hysteresis with a modified goman-khrabrov model on pitching airfoils, 45th AIAA Fluid Dynamics Conference (2015) 2631.